

Supporting Information

Exciton-Plasmon Polariton Coupling and Hot Carrier Generation in 2D SiB Semiconductors: **A First-Principles Study**

Ali Ramazani¹, Farzaneh Shayeganfar², Jaafar Jalilian³, Nicholas X. Fang¹

¹Department of Mechanical Engineering, Massachusetts Institute of Technology, Cambridge, MA, USA

²Department of Civil and Environmental Engineering, Rice University, Houston, TX, 77005, USA

³Department of Physics, College of Sciences, Yasouj University, Yasouj 75914-353, Iran

S1 Phonon calculations

Phonon dispersion calculations are carried out using density functional perturbation theory (DFPT) [S1] as implemented in the QUANTUM ESPRESSO package [S2] to check the dynamical stability of the monolayer. The valence electron wave functions are expanded using an energy cut-off of 100 Ry and a Martin-Troullier norm-conserving pseudopotential [S3] is used to treat the core electrons. The phonon band structures are calculated along the high symmetry path Γ –M–K– Γ .

The phonon spectrum for both SiB and H-SiB monolayers are shown in **Fig. S1**. As can be **seen** in this figure, only the H-SiB monolayer is dynamically stable. Indeed, semi-hydrogenation leads to improved stability of SiB monolayers and also increases the maximum of the vibrational frequency from $\omega_{\max}(\text{SiB}) = 854\text{cm}^{-1}$ to $\omega_{\max}(\text{H-SiB}) = 1984\text{cm}^{-1}$.

There are multiple procedures to modify the dynamical stability of nanomaterials such as doping [S4], addition of extra layers [S5] and surface functionalization [S6, S7]. To improve the dynamical stability of the SiB honeycomb monolayer, surface functionalization has been used, which is a fruitful approach for stabilizing low-dimensional nanostructures. While the functionalization could change the out-of-plane vibrations and stabilize the structure, it could also change the electronic properties of the SiB monolayer. As can be seen in **Fig. S1 B**, the SiB monolayer becomes stable after semi-homogenization.

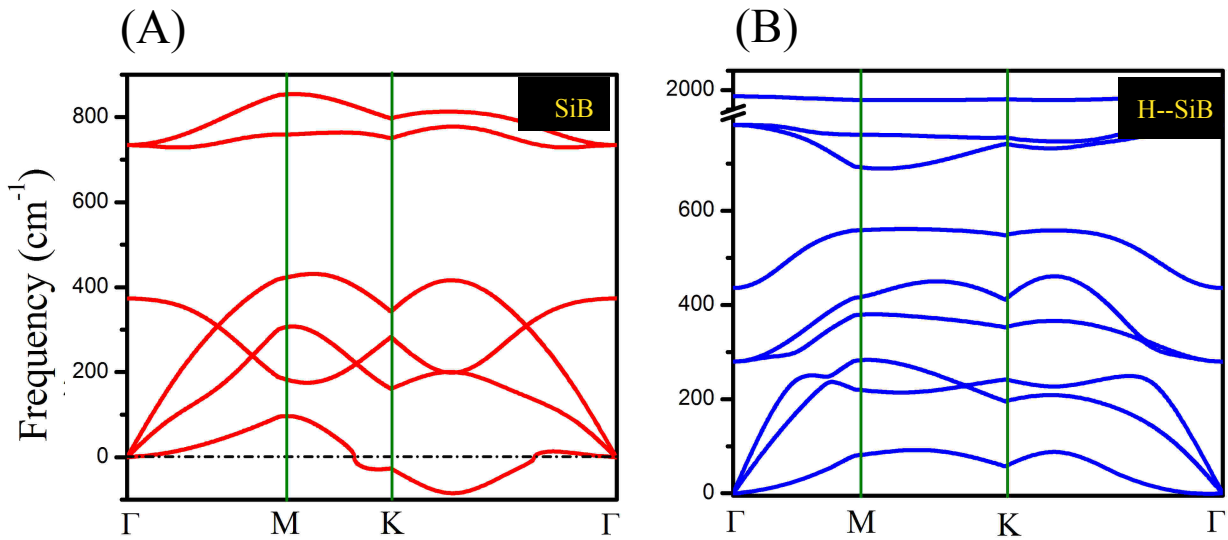


Fig. S1: Phonon dispersion for (A) pure and (B) semi-hydrogenated (hydrogen absorbed on Si atoms) SiB graphene-like monolayer.

S2 Mechanical Properties

Bandgap engineering is a powerful technique to design new semiconducting materials. Strain engineering as a concept for tuning the bandgap exploits to alter the physical and chemical properties of materials, and make them promising potential candidates for photonic devices.

In this section, we studied mechanical properties of both SiB and H-SiB monolayers. This is very important since the strain field is a significant agent used to modulate the bandgap of materials in order to create photo-devices with spatial variation in the electronic structure. The strain-stress curve for both SiB and H-SiB monolayers is plotted in **Fig. S2**. As can be seen in this Fig., the stress-strain behavior of both SiB and H-SiB monolayers are linear till 6% strain; therefore, we will apply biaxial strain up to 6% to H-SiB monolayer to investigate the effect of strain field on the electronic and optical properties of the system.

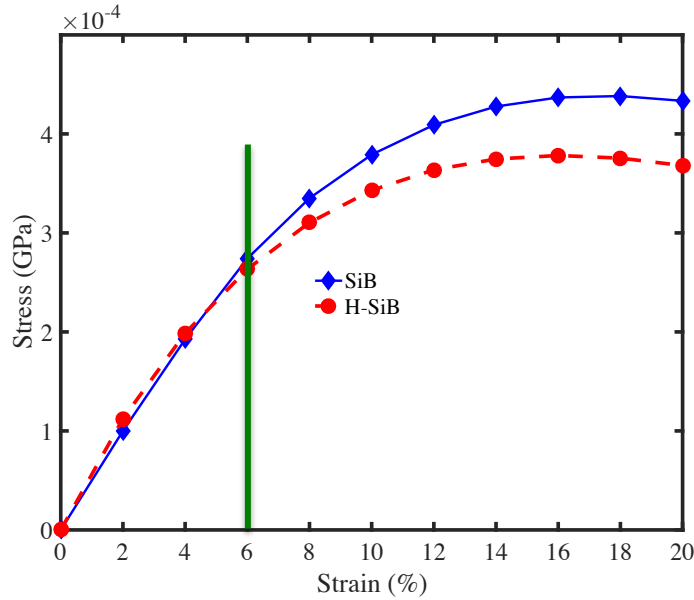


Fig. S2: Strain-Stress diagram for SiB and H-SiB monolayers. The green line shows the maximum strain, up to which, the stress-strain behavior is linear. Therefore, the SiB and H-SiB monolayers are subjected up to 6% deformation in this study.

S3 GW approach

The GW approximation computes quasiparticle (QP) energies (ϵ_i) and wavefunctions (ϕ_i) solving Dyson equation for one electron added or removed from the material [S8]:

$$H_0 \varphi_i(\mathbf{r}) + \int \Sigma(\mathbf{r}, \mathbf{r}') \varphi_i(\mathbf{r}') d^3\mathbf{r}' = \varepsilon_i \varphi_i(\mathbf{r}) \quad (\text{S1})$$

where Σ is the self-energy operator of electron–electron (e-e) interactions, and is approximated in the screened Coulomb interaction, W , as below [S8]:

$$\Sigma(\mathbf{r}, \mathbf{r}'; \omega) \cong \frac{i}{2\pi} \int G(\mathbf{r}, \mathbf{r}'; \omega) W(\mathbf{r}, \mathbf{r}'; \omega + \omega') e^{i\delta\omega} d\omega' \quad (\text{S2})$$

where G is the one particle electronic Green's function, and δ is a converging factor [S8]:

$$G(\mathbf{r}, \mathbf{r}'; \omega) = \sum_i \frac{\varphi_i(\mathbf{r}) \varphi_i^*(\mathbf{r}')}{\omega - \varepsilon_i} \quad (\text{S3})$$

$$W(\mathbf{r}, \mathbf{r}'; \omega) = \frac{1}{\Omega} \int \epsilon^{-1}(\mathbf{r}, \mathbf{r}'; \omega) V^c(\mathbf{r}'' - \mathbf{r}') d\mathbf{r}'' \quad (\text{S4})$$

where ϵ is the dielectric function within RPA ($\epsilon^{\text{RPA}}(\mathbf{q}, \omega) = 1 - V(\mathbf{q}) \chi^0(\mathbf{q}, \omega)$, where χ^0 polarizability), and V^c is the Coulomb potential [S9]. A first-order correction to Kohn-Sham (K-S) lead to compute quasiparticle energies ($E_{\text{nk}}^{\text{QP}}$) [S8],

$$E_{\text{nk}}^{\text{QP}} = E_{\text{nk}}^{\text{DFT}} + \langle \text{nk} | \Sigma(E_{\text{nk}}^{\text{QP}}) | \text{nk} \rangle - \langle \text{nk} | V_{\text{xc}}^{\text{DFT}} | \text{nk} \rangle \quad (\text{S5})$$

Where n , and k are the band index and electron wave vector, respectively. $V_{\text{xc}}^{\text{DFT}}$ is the DFT exchange-correlation potential.

S4 Beth-Salpeter Equation (BSE)

To find excitation energies, we solved the BSE, which takes into account electron–hole (e-h) interactions using the perturbation theory. The BSE is defined as [S8]:

$$(E_{\text{ck}}^{\text{QP}} - E_{\text{vk}}^{\text{QP}}) A_{\text{vcK}}^{\text{S}} + \sum_{\text{v'c'K'}} \langle \text{vcK} | K^{\text{eh}} | \text{v'c'K'} \rangle A_{\text{v'c'K'}}^{\text{S}} = \Omega^{\text{S}} A_{\text{vk}}^{\text{S}} \quad (\text{S6})$$

where Ω is the eigenvalue of the S state, and $A_{\text{vcK}}^{\text{S}}$ are the coupling coefficients between valence (v) and conduction (c) QP states. K^{eh} is the e–h interaction kernel, which is composed of direct and exchange terms as $K^{\text{eh}} = K^{\text{D}} + K^{\text{X}}$; where K^{D} and K^{X} are the e–h attraction and repulsive exchange terms, respectively [S8].

To get the ground state of the atomic structures of unstrained and strained H-SiB monolayers, we utilized DFT calculations with Perdew, Burke, and Ernzerhof (PBE) exchange correlation functional within generalized-gradient approximation (GGA). To optimize the geometry, we set the convergence criteria of 10^{-4} eV for the total energy, and 10^{-3} eV/Å for the ionic force. To get a precise electronic band structure, we chose $12 \times 12 \times 1$ for Monkhorst–Pack k-sampling.

To characterize the optical excitation energies, the BSE is solved taking into account the electron-hole (e-h) interaction. In fact, the complex transverse dielectric function, $\epsilon(E) = \epsilon_1(E) + i\epsilon_2(E)$ is computed using GW/ BSE within the Tamm-Dancoff and static approximations. The extinction and refractive index are defined as [S10]:

$$k(E) = \frac{1}{\sqrt{2}} \sqrt{-\epsilon_1(E) + \sqrt{\epsilon_1^2(E) + \epsilon_2^2(E)}} \quad (S7)$$

$$n(E) = \frac{1}{\sqrt{2}} \sqrt{\epsilon_1(E) + \sqrt{\epsilon_1^2(E) + \epsilon_2^2(E)}} \quad (S8)$$

and the standard expression for absorption and reflectivity are calculated via [S10]:

$$\alpha(E) = \frac{4\pi E k(E)}{hc} \quad \& \quad R(E) = \frac{(n-1)^2 + k^2}{(n+1)^2 + k^2} \quad (S9)$$

The plane wave energy cutoff for the DFT calculations was set to 720 eV. To build the dielectric function, the total number of states is 2400, which spans energies greater than 40 eV. The dielectric function plane wave cut-off is 240 eV. The summation of BSE was computed using 16 valence \times 16 conduction states for H-SiB.

The exciton energy, and exciton wave function $\psi(r_e, r_h)$ are calculated from BSE. To obtain the spatial distribution of excitons ($F(r)$), we use the correlation function of hole and electron, where electrons and holes are separated by a vector (r) as [S11]:

$$F(r) = \int_{\Omega} d^3r_h |\psi(r_e = r_h + r, r_h)|^2 \quad (S10)$$

where r_e and r_h are the electron and hole coordinates, respectively; and Ω is the volume of a primitive cell. We utilized BGW package [S9, S12, S13] to compute the imaginary and real part of dielectric function (ϵ_2 and ϵ_1), and accordingly, calculate the absorption and reflectivity spectrum of the material.

S5 Photovoltaic conversion efficiency

The bandgap energies and significant optical absorbance in visible range of unstrained and strained H-SiB suggest that H-SiB is a good candidate for the use in the new generation of ultrathin solar cells. To calculate the fraction of sunlight converted to electrical power density as photovoltaic conversion efficiency for strained H-SiB monolayers, the optical absorption and reflectivity coefficient are two major parameters, which can affect the photovoltaic efficiency. The photovoltaic conversion efficiency is acquired by integrating the spectral irradiance over photon wavelength (λ) as [S10]:

$$P = \int_0^{\lambda_{max}} W(\lambda)[1 - R(\lambda)]C(\lambda)A(\lambda)d\lambda \quad (S11)$$

where λ_{max} is the maximum wavelength absorbed by semi-hydrogenated SiB, $W(\lambda)$ is the solar irradiance spectrum via AirMass as 1.5 [S14], $R(\lambda)$ is the reflectivity coefficient as described in **Eq. S9**, and $A(\lambda)$ is the absorbance defined as $(A(\lambda) = 1 - e^{-\alpha(\lambda)d})$ [S10]; and d is the thickness of the nanostructure. In **Eq. S11**, $C(\lambda)$ accounts the fraction of excitation energy of excitons (electron-hole pair) converted to the electrical energy; $C(\lambda) = E_g\lambda/hc$; E_g is the bandgap energy (direct or indirect).

2D materials are considered as the future generation of photovoltaic materials due to their higher density of states and exciting optical and electronic properties, which causes more significant absorption of photons in comparison to bulk materials [S15, S16]. In fact, 2D materials and thin films gain and collect more photons by light scattering particles, because they capture incident

light. Therefore, 2D solar cells can enhance the photoexcited carrier collection by an improved charge carrier diffusion [S15]. **Fig. S3** shows the electrical power of H-SiB relative to the bulk Si with a thickness of 100 nm as a function of strained H-SiB. The data trend reveals that conversion electrical power for H-SiB is 2.7 times (photovoltaic efficiency 3.8 %) greater than bulk Si. Moreover, taking into account electron-hole interaction enhances the photovoltaic conversion efficiency.

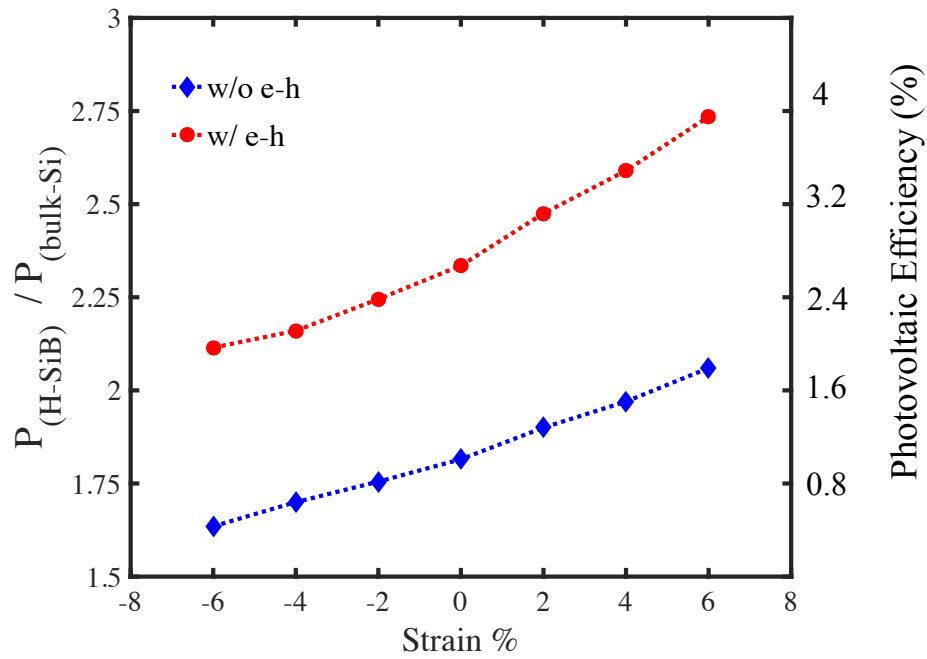


Fig. S3: Electrical power for semi-hydrogenated SiB (H-SiB) relative to Bulk Si as a function of strained H-SiB. The data trend reveals that conversion electrical power for H-SiB without/with strain is greater than bulk Si. Moreover, taking into account electron-hole interaction enhances photovoltaic efficiency.

S6 Effective Hamiltonian (H-SiB)

In this section, we model the σ , π and π^* band energy dispersion of H-SiB using a second nearest

neighbor (NN) tight-binding (TB) Hamiltonian as shown in **Fig. S4**. TB Hamiltonian takes into account all valence electrons; i.e. one s and two p electrons for B atom (three), one s and three p electrons for Si atom (four) and one s of H atom. The TB Hamiltonian is [S17]: $H = H_0 + H_1 + H_2$; where H_0 , H_1 and H_2 take into account the on-site energy, first NN, and second NN in the structure, respectively. H_0 is described as follows [S17]:

$$H_0 = \sum_i (\varepsilon_s a_i^\dagger a_i + \varepsilon_p \sum_\alpha (b_{i\alpha}^\dagger b_{i\alpha}) + \varepsilon_s^H c_i^\dagger c_i) \quad (\text{S12})$$

where ε_s represents on-site energy of the s orbitals of Si/B, ε_p is on-site energy of p orbitals of Si/B, and ε_{sH} is the on-site energy of the s electron orbital of the hydrogen atom. Here, a^\dagger/b^\dagger and a/b are the creation and annihilation operators of the s/p electrons of Si/B; while c^\dagger and c are the creation and annihilation operators for H atoms. H_1 has the following form [S17]:

$$H_1 = \sum_i (\gamma_{sHs} c_i^\dagger a_i) + \gamma_{ss} a_A^\dagger a_B + \sum_\alpha (\gamma_{sp} v_\alpha^{AB} a_A^\dagger b_{B\alpha} + \gamma_{pp\sigma} (v_\alpha^{AB})^2 b_{A\alpha}^\dagger b_{B\alpha} + \gamma_{pp\pi} (1 - (v_\alpha^{AB})^2) b_{A\alpha}^\dagger b_{B\alpha}) + \sum_{\alpha \neq \beta} (\gamma_{pp\sigma} v_\beta^{AB} b_{A\alpha}^\dagger b_{B\beta} - \gamma_{pp\pi} v_\alpha^{AB} v_\beta^{AB} b_{A\alpha}^\dagger b_{B\alpha} + \sum_\alpha \gamma_{sHp} v_\alpha^{AB} c_A^\dagger b_{B\alpha}) + h.c. \quad (\text{S13})$$

where γ_{sHp} is a representative of the first and second NN, which hopes between s orbitals of Si/B and hydrogen. γ_{ss} , γ_{sp} , $\gamma_{pp\sigma}$, and $\gamma_{pp\pi}$ are the first NN hopping between s and p orbitals and their mixing with σ , π bonding electrons of Si/B on sub-lattices A and B. H_2 becomes [S17]:

$$H_2 = \sum_i (\gamma'_{ss} a_i^\dagger a_{i'} + \sum_\alpha (\gamma'_{sp} v_\alpha^{AA'} a_i^\dagger b_{i'\alpha} + \gamma'_{pp\sigma} (v_\alpha^{AA'})^2 b_{A\alpha}^\dagger b_{A'\alpha} + \gamma'_{pp\pi} (1 - (v_\alpha^{AA'})^2) b_{A\alpha}^\dagger b_{A'\alpha}) + \sum_{\alpha \neq \beta} (\gamma'_{pp\sigma} v_\alpha^{AA'} v_\beta^{AA'} b_{A\alpha}^\dagger b_{A'\beta} - \gamma'_{pp\pi} v_\alpha^{AA'} v_\beta^{AA'} b_{A\alpha}^\dagger b_{A'\beta} + \gamma'_{sHs} c_A^\dagger a_B + \sum_\alpha \gamma'_{sHp} v_\alpha^{AB'} c_A^\dagger b_{B\alpha}) h.c. \quad (\text{S14})$$

Where v_α^{AB} , $v_\alpha^{AA'}$, $v_\alpha^{AB'}$ are:

$$v_\alpha^{AB} = \frac{(R_{Si/B}^A - R_{Si/B}^B)_\alpha}{|(R_{Si/B}^A - R_{Si/B}^B)_\alpha|}, \quad v_\alpha^{AA'} = \frac{(R_{Si/B}^A - R_{Si/B}^{B'})_\alpha}{|(R_{Si/B}^A - R_{Si/B}^{B'})_\alpha|}, \quad v_\alpha^{AB'} = \frac{(R_{Si/B}^A - R_H^{B'})_\alpha}{|(R_{Si/B}^A - R_H^{B'})_\alpha|} \quad (\text{S15})$$

γ'_{ss} , γ'_{sp} , $\gamma'_{pp\sigma}$, and $\gamma'_{pp\pi}$ are the second-NN hopping between the Si/B s and p orbitals and their mixing with σ , π bonding electrons on the same sub-lattice.

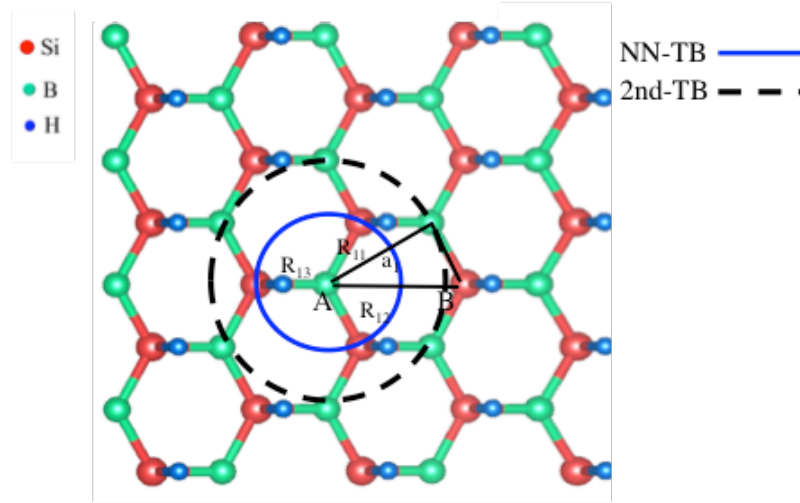


Fig. S4: The crystallographic structure of monolayer H-SiB. As can be seen, the nearest neighbor (NN), second NN are shown for tight binding Hamiltonian (TB) model development.

γ'_{sHs} and γ'_{sHp} are the second-NN hopping between the s and p orbitals of Si/B and s orbital of hydrogen on different sub-lattices. Summations in α and β go over x, y, z, in i goes over the A and B sub-lattices, respectively. v_{α}^{AB} , $v_{\alpha}^{AA'}$, and $v_{\alpha}^{AB'}$ are orientations of the p orbitals (p_x, p_y, p_z). \mathbf{R} denotes the coordinates of the atoms. The TB Hamiltonian elements are given in the method section. The TB Hamiltonian for H-SiB can be written as [S17]:

$$\begin{pmatrix}
H'_{ss} & H'_{sx} & H'_{sy} & H'_{sz} & \left| \begin{array}{cccc} H_{ss} & H_{sx} & H_{sy} & H_{sz} \\ H_{sx} & H_{xx} & H_{xy} & H_{xz} \\ H_{sy} & H_{xy} & H_{yy} & H_{yz} \\ H_{sz} & H_{xz} & H_{yz} & H_{zz} \end{array} \right| & H_{sHs} & H'_{sHs} \\
H'^*_{ss} & H'^*_{sx} & H'^*_{sy} & H'^*_{sz} & \left| \begin{array}{cccc} H'_{ss} & H'_{sx} & H'_{sy} & H'_{sz} \\ H'^*_{ss} & H'^*_{sx} & H'^*_{sy} & H'^*_{sz} \\ H'^*_{sx} & H'^*_{xx} & H'^*_{xy} & H'^*_{xz} \\ H'^*_{sy} & H'^*_{xy} & H'^*_{yy} & H'^*_{yz} \\ H'^*_{sz} & H'^*_{xz} & H'^*_{yz} & H'^*_{zz} \end{array} \right| & H'_{sHs} & H_{sHs} \\
H'^*_{sx} & H'^*_{xx} & H'^*_{xy} & H'^*_{xz} & \left| \begin{array}{cccc} H'^*_{ss} & H'^*_{sx} & H'^*_{sy} & H'^*_{sz} \\ H'^*_{sx} & H'^*_{xx} & H'^*_{xy} & H'^*_{xz} \\ H'^*_{sy} & H'^*_{xy} & H'^*_{yy} & H'^*_{yz} \\ H'^*_{sz} & H'^*_{xz} & H'^*_{yz} & H'^*_{zz} \end{array} \right| & H'_{sHx} & H'_{sHx} \\
H'^*_{sy} & H'^*_{xy} & H'^*_{yy} & H'^*_{yz} & \left| \begin{array}{cccc} H'^*_{ss} & H'^*_{sx} & H'^*_{sy} & H'^*_{sz} \\ H'^*_{sx} & H'^*_{xx} & H'^*_{xy} & H'^*_{xz} \\ H'^*_{sy} & H'^*_{xy} & H'^*_{yy} & H'^*_{yz} \\ H'^*_{sz} & H'^*_{xz} & H'^*_{yz} & H'^*_{zz} \end{array} \right| & H'_{sHy} & H'_{sHy} \\
H'^*_{sz} & H'^*_{xz} & H'^*_{yz} & H'^*_{zz} & \left| \begin{array}{cccc} H'^*_{ss} & H'^*_{sx} & H'^*_{sy} & H'^*_{sz} \\ H'^*_{sx} & H'^*_{xx} & H'^*_{xy} & H'^*_{xz} \\ H'^*_{sy} & H'^*_{xy} & H'^*_{yy} & H'^*_{yz} \\ H'^*_{sz} & H'^*_{xz} & H'^*_{yz} & H'^*_{zz} \end{array} \right| & H'_{sHz} & H_{sHp} \\
H^*_{sHs} & & & H^*_{sHp} & \left| \begin{array}{cccc} H'^*_{ss} & H'^*_{sx} & H'^*_{sy} & H'^*_{sz} \\ H'^*_{sx} & H'^*_{xx} & H'^*_{xy} & H'^*_{xz} \\ H'^*_{sy} & H'^*_{xy} & H'^*_{yy} & H'^*_{yz} \\ H'^*_{sz} & H'^*_{xz} & H'^*_{yz} & H'^*_{zz} \end{array} \right| & H'_{sHSH} & \\
H'^*_{sHs} & H'^*_{sHx} & H'^*_{sHy} & H'^*_{sHz} & \left| \begin{array}{cccc} H'^*_{ss} & H'^*_{sx} & H'^*_{sy} & H'^*_{sz} \\ H'^*_{sx} & H'^*_{xx} & H'^*_{xy} & H'^*_{xz} \\ H'^*_{sy} & H'^*_{xy} & H'^*_{yy} & H'^*_{yz} \\ H'^*_{sz} & H'^*_{xz} & H'^*_{yz} & H'^*_{zz} \end{array} \right| & H'^*_{sHSH} & H'_{sHs}H
\end{pmatrix} \quad (S16)$$

The Hamiltonian elements are defined as [S17]:

$$H_{ss} = \gamma_{ss} \sum_B e^{ik(R_{B,si}^A - R_{B,si}^B)}, H_{sHs} = \gamma_{sHs}, H_{sHp} = \gamma_{sHp} \quad (S17)$$

$$H_{s\alpha} = \gamma_{sp} \sum_B v_{\alpha}^{AB} e^{ik(R_{B,si}^A - R_{B,si}^B)}, H'_{s\alpha} = \gamma'_{sp} \sum_A v_{\alpha}^{AB} e^{ik(R_{B,si}^A - R_{B,si}^{A'})} \quad (S18)$$

$$H_{\alpha\alpha} = \gamma_{pp\sigma} \sum_B (v_{\alpha}^{AB})^2 e^{ik(R_{B,si}^A - R_{B,si}^B)} + \gamma_{pp\pi} \sum_B (1 - (v_{\alpha}^{AB})^2) e^{ik(R_{B,si}^A - R_{B,si}^{A'})} \quad (S19)$$

$$H_{\alpha\beta} = \gamma_{pp\sigma} \sum_B v_{\alpha}^{AB} v_{\beta}^{AB} e^{ik(R_{B,si}^A - R_{B,si}^B)} - \gamma_{pp\pi} \sum_B v_{\alpha}^{AB} v_{\beta}^{AB} e^{ik(R_{B,si}^A - R_{B,si}^B)}, \alpha \neq \beta \quad (S20)$$

$$H'_{\alpha\alpha} = \varepsilon_p + \gamma'_{pp\sigma} \sum_A (v_{\alpha}^{AA'})^2 e^{ik(R_{B,si}^A - R_{B,si}^{A'})} + \gamma'_{pp\pi} \sum_B (1 - (v_{\alpha}^{AA'})^2) e^{ik(R_{B,si}^A - R_{B,si}^{A'})} \quad (S21)$$

$$H'_{\alpha\beta} = \gamma'_{pp\sigma} \sum_A v_{\alpha}^{AA'} v_{\beta}^{AA'} e^{ik(R_{B,si}^A - R_{B,si}^{A'})} - \gamma'_{pp\pi} \sum_{BA} v_{\alpha}^{AA'} v_{\beta}^{AA'} e^{ik(R_{B,si}^A - R_{B,si}^{A'})}, \alpha \neq \beta \quad (S22)$$

$$H'_{sHs} = \gamma'_{sHs} \sum_B e^{ik(R_{B,si}^A - R_{B,si}^{B'})}, H'_{sHSH} = \varepsilon_s^H + \gamma'_{sHSH} \sum_A e^{ik(R_{B,si}^A - R_{B,si}^{A'})} \quad (S23)$$

$$H'_{sH\alpha} = \gamma'_{sHs} \sum_B v_{\alpha}^{AB'} e^{ik(R_{B,si}^A - R_{B,si}^{B'})}, H'_{ss} = \varepsilon_s + \gamma'_{ss} \sum_A e^{ik(R_{B,si}^A - R_{B,si}^{A'})} \quad (S24)$$

Though the total number of parameters in this TB model is 17, only 5 parameters should be set to zero. **Eqs. S16-S24** are solved simultaneously in MATLAB (R2016a, The MathWorks Inc., Natick, MA, USA) to obtain the other 12 parameters, which can produce the exact same electronic structure of H-SiB developed by first-principles GW-DFT.

The total number of parameters in this TB model is 17, but 5 parameters are zero such as $\gamma'_{pp\pi}$, γ_{sHp} because of creation of σ bond between hydrogen and Si-3p_z (σ_{Si-H}). The 12 parameters can be treated as semiempirical of reproduction of first-principles (DFT) band structures implemented in the GW (see **Fig. S5**). Resulting parameters are brought in **Table S1**.

Table S1. Parameters of TB model compared with GW band structure.

TB-Hamiltonian parameters (eV)	ϵ_s	ϵ_p	ϵ_{sH}	γ_{ss}	γ_{sp}	$\gamma_{pp\sigma}$	γ'_{ss}	γ'_{sp}	$\gamma'_{pp\sigma}$	γ'_{sHsH}	γ'_{sHs}	γ'_{sHp}
	-6.45	-4.55	-2.34	-1.23	-2.47	-3.12	0.38	0.07	0.4	0.04	0.42	-0.06

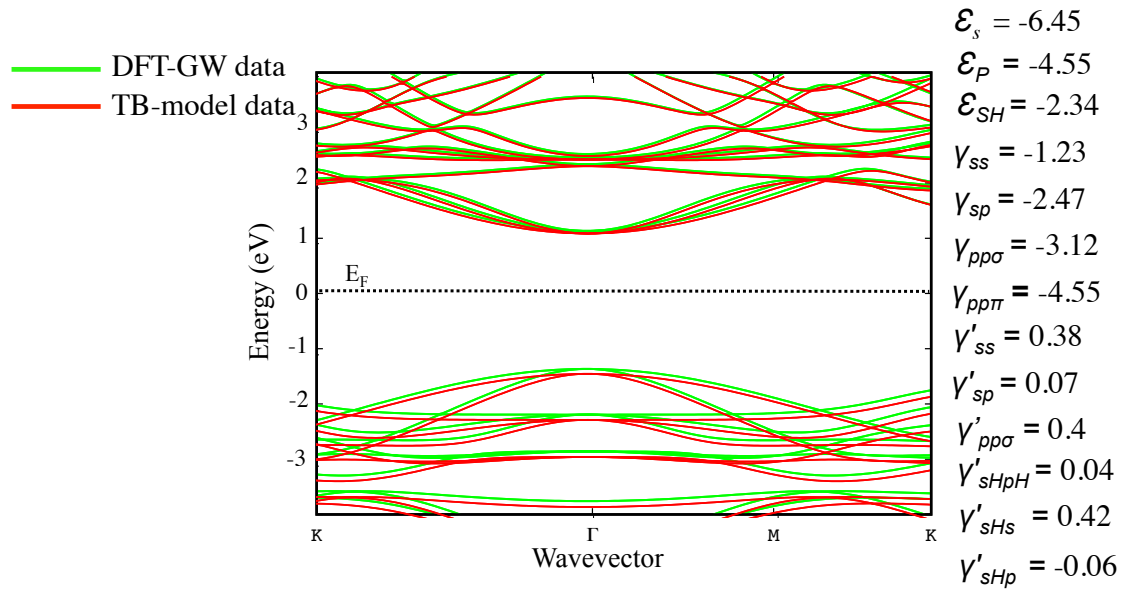


Fig. S5: Comparison between band structures developed by TB and GW. The parameters of TB model are shown in the legend (unit is eV).

S7 Polarizability matrix $\chi(\mathbf{q},\omega)$ (density-density response function)

The Kohn–Sham (KS) orbitals based upon plane waves basis is [S18]:

$$\phi_{n\mathbf{k}}(r) = \frac{1}{\Omega} \sum_{\mathbf{G}} C_{n\mathbf{k}}(\mathbf{G}) e^{i(\mathbf{k}+\mathbf{G})\cdot\mathbf{r}} \quad (\text{S25})$$

where \mathbf{G} is the reciprocal lattice, \mathbf{K} represents quasi-wavevectors (QW) of the first Brillouin zone (BZ) and Ω is the crystal volume.

To formulate the many body electronic properties of 2D systems, non-interacting $\chi^0(\mathbf{q},\omega)$, and interacting $\chi(\mathbf{q},\omega)$ polarizability are the main parameters in the calculation of exciton-Plasmon interaction [S19]. A density-density response function of non-interacting 3D electrons in the reciprocal space is obtained from Adler–Wiser periodic [S20]:

$$\chi_{GG'}^0(\mathbf{q}, \omega) = \frac{2}{\Omega} \sum_{\mathbf{k}, \nu, \nu'} \frac{f_{\nu}(\mathbf{k}) - f_{\nu'}(\mathbf{k}+\mathbf{q})}{\hbar\omega + \varepsilon_n(\mathbf{k}) - \varepsilon_m(\mathbf{k}+\mathbf{q}) + i\eta} \rho_{\nu\nu'}^{k\mathbf{q}}(\mathbf{G}) \rho_{\nu\nu'}^{k\mathbf{q}}(\mathbf{G}')^* \quad (\text{S26})$$

where \mathbf{G} and \mathbf{G}' are the reciprocal lattice vectors, ω is the frequency, and $\varepsilon_n(\mathbf{k})$ is the empty bands and $\varepsilon_m(\mathbf{k} + \mathbf{q})$ is the filled bands, while $f_n(\mathbf{k}) = \theta(E_F - \varepsilon_n(\mathbf{k}))$ is the Fermi-Dirac distribution. $\rho_{\nu\nu'}^{k\mathbf{q}}(\mathbf{G})$ is the matrix element and has a form of [S18]:

$$\rho_{\nu\nu'}^{k\mathbf{q}}(\mathbf{G}) = \langle \Phi_{\nu\mathbf{k}} | e^{-i(\mathbf{q}+\mathbf{G})\cdot\mathbf{r}} | \Phi_{\nu'\mathbf{k}+\mathbf{q}} \rangle_{\Omega} \quad (\text{S27})$$

where $\Phi_{\nu\mathbf{k}}(r)$ is the KS electron wave function with \mathbf{q} as a momentum transfer vector. The expression of interacting polarizability $\chi_{GG'}$ is a density-response function as [S20]:

$$\chi_{GG'} = \chi_{GG'}^0 + \sum_{G_1 G_2} \chi_{GG'}^0 \chi_{G_1 G_2} \chi_{G_2 G'} \quad (\text{S28})$$

where $v_{G_1 G_2}$ is a representative the Fourier coefficients of e-e interactions of two reciprocal lattice vectors (G_1 and G_2). In the electron liquid, the bare Coulomb interaction is given by $v_{GG'}^0 = 4\pi e^2 \delta_{GG'} / \epsilon |\mathbf{q} + \mathbf{G}|^2$ where ϵ is the average dielectric constant of the environment. In all our numerical results, we consider $\epsilon = 1$. The alternative representation of the polarizability (χ) is given by $\chi^0 \epsilon^{-1}$. ϵ is the RPA dielectric matrix and described as $\epsilon = I - V \chi^0$ [S21, S22]; where I is the identity matrix, V is the matrix of the Coulomb potential ($V = \frac{e^2}{|R_I - R_j|}$) [S23], and χ^0 is the independent-particle susceptibility matrix, which is defined by **Eq. S26**, and includes the matrix element of electronic states (eigenvectors and eigenstates). In the RPA approach, an approximation in the high-density limit becomes valid when the electron interactions are considered as the only parameter to produce the screening field. The response to such a screened field is measured by χ^0 . On the other hand, the main assumption in RPA is to consider the electrons response function as an effective potential [S18]. The bare Coulomb potential is also given by $v_{GG'}^0 = 4\pi e^2 \delta_{GG'} / \epsilon |\mathbf{q} + \mathbf{G}|^2$. The long-range Coulomb interaction between repeated planar arrays are described as [S18]:

$$v_{GG'}^0 = \frac{2\pi e^2 \delta_{gg'}}{|\mathbf{q} + \mathbf{g}|} \int_{-L/2}^{L/2} dz \int_{-L/2}^{L/2} dz' e^{i(G_z z - G'_z z') - |\mathbf{q} + \mathbf{g}| |z + z'|} \quad (\text{S29})$$

where g and G_z are in-plane and out-plane components of G . The external perturbation in the system based on the linear response theory creates an excitation carrier state of energy ($\hbar\omega$) and wave vector ($\mathbf{q} + \mathbf{G}$), which are the diagonal elements of the RPA dielectric function ($\epsilon_{GG'}$) [S18]:

$$\epsilon_{GG'} = \delta_{GG'} - \sum_{G_1} \chi_{GG'}^0 v_{G_1 G'}^0 \quad (\text{S30})$$

The plasmon modes can be obtained when the real part of dielectric function ($\mathcal{E}(q, \omega)$) is set to zero [S18]:

$$\mathcal{E}(q, \omega) = \frac{1}{(\mathcal{E}^{-1})_{GG'}} |G = G' = 0 \quad (\text{S31})$$

Accordingly, the electron energy loss (EEL) function is considered as the imaginary part of the inverse of the dielectric function $\mathcal{E}(q, \omega)$ as[S24, S25]:

$$E_{EEL}(q, \omega) = -\Im m[1/\mathcal{E}(q, \omega)] \quad (\text{S32})$$

The nonlocal field effects appear in EEL as off-diagonal elements of $\chi_{GG'}$ [S24]. To describe the light-matter interaction, we used non-local conductivity in terms of polarizability matrix (density-density response function) through the following relation:

$$\sigma(q, \omega) = \frac{ie^2\omega}{q^2} \chi(q, \omega) \quad (\text{S33})$$

Eqs. S31-S33 are utilized to study the optoelectronic properties of 2D crystalline materials. **In practice, to acquire the polarizability matrix, we first calculated the electronic eigenvalues and eigenvectors using a mean field code, then the static and dynamic RPA polarizability ($\chi_{GG'}$) and corresponding inverse dielectric function were computed using BerkeleyGW [S13].**

S8 Self-Energy (Σ)

To compute the real and imaginary parts of the electron-electron (e-e) self-energy ($\Sigma_{n,k}^{e-e}$) [S12], we use BGW [S11, S13]. Plasmon pole calculation on a $14 \times 14 \times 1$ k-point grid gives the $\text{Re } \Sigma_{n,k}^{e-e}$ and then interpolated using Wannier functions. Screened kinetic energy cutoff was set to 75 Ry and Coulomb interaction cut off was set to 160 Ry in conjunction with 500 empty bands and a $12 \times 12 \times 1$ q-point grid for the dielectric screening. The imaginary part of the e-e self-energy,

$\text{Im } \Sigma_{n,k}^{e-e}$ is computed using full frequency GW calculations [S11-S13]. Here $\text{Im } \Sigma_{n,k}^{GW}$ are evaluated on-shell at the LDA eigenvalues $E_{n,k}$, and then plotted versus the corresponding GW eigenvalues $E_{n,k}$. We used fine K-point $18 \times 18 \times 1$, converging $\text{Im } \Sigma_{n,k}^{GW}$ within ~ 8 meV. For bare Coulomb interactions and kinetic energy cutoffs, we used the same values of Real part, and with ~ 200 empty bands and for dielectric screening a $18 \times 18 \times 1$ q-point was set.

To compute the imaginary part of the electron-phonon (e-ph) self-energy, $\text{Im } \Sigma_{n,k}^{e-ph}$, we employed the EPW code [S26]. We compute the self-consistent (scf) and non-scf potential on a $12 \times 12 \times 1$ k-point grid using DFT, and phonon lattice-dynamical properties with on a coarse $6 \times 6 \times 1$ q-point grid in the first step. In the second step, by tacking fine q-grid interpolate KS states based on Wannier functions as implemented in the EPW code. Maximally localized Wannier functions [S27] are obtained starting from three p and two s orbitals on the Si/B, for a total of five wannierized bands within $-4 \dots 4$ eV of Fermi energy. By sampling fine k-point $36 \times 36 \times 1$ and lots of random phonon q-points in the BZ.

We compute $\text{Im } \Sigma_{n,k}^{e-ph}$, converging within 1 meV. Further computation details for e-ph self-energy are discussed in ref [S28]. The temperature dependent $\text{Im } \Sigma_{n,k}^{e-ph}$ are carried out by using EPW code [S26-S29].


Boson-electron Coupling matrix parameters, and effect of temperature on the polarizability and self-energy are explained in **S4** and **S5** of **SI**, respectively.

S9 Boson-electron Coupling matrix parameters

The square modulus of the coupling matrix element of boson-electron ($|g|^2$) of plasmon-electron ($|g^{PL}|^2$) is given in **Table S2**. The details of the derivation of photon-electron coupling matrix ($|g_{n,n',k}^{PH}|^2$), and SPP–electron coupling matrix ($|g_{n,n',k}^{SPP}|^2$) are beyond of the scope of this paper.

However, the interested readers can find the details in Ref. [S30].

Table S2. Feynman diagram for the Σ (self-energy) and $|g|^2$ as square modulus of the coupling matrix element of three bosons ($|g^{PL}|^2$, $|g_{n,n',k}^{PH}|^2$, and $|g_{n,n',k}^{SPP}|^2$, which are the plasmon-electron, photon-electron, and surface plasmon polariton (SPP), respectively). The Feynman diagram consists of a polarizability bubble χ multiplied by two coupling vertices g [S30].

Interaction	Matrix elements	
Plasmon-electron	$ g^{PL} ^2 = 2\pi \frac{e^2 E_p}{q_p^2}$	
Photon-electron	$ g_{n,n',k}^{PH} ^2 = \left(\frac{e\hbar}{m}\right)^2 \left(1/(2\epsilon E_p V)\right) \left e_{q_p} \cdot P_{n,n',k}(q_p = 0)\right ^2$	
SPP-electron	$ g_{n,n',k}^{SPP} ^2 = \left(\frac{e\hbar}{m}\right)^2 \left(1/(2\epsilon_{eff} E_p A L_z)\right) \left e_{q_p}^{TM} \cdot P_{n,n',k}(q_p)\right ^2$	

S10 Effect of temperature on the polarizability and self-energy

To understand the temperature effect on the self-energy, we utilized an approach recently introduced by Ponce et al. [S31], in which the role of finite temperature in the self-energy of materials is described and implemented in a package named EPW [S32]. The equations for electron and phonon self-energies are explained in details in the next section.

Electron and phonon self-energies: To compute the first order of electron-phonon (e-ph) matrix, we used density functional perturbation theory (DFPT) as [S28]:

$$g_{mn,v}(\mathbf{k}, \mathbf{k}') = \frac{1}{\sqrt{2\omega_{\mathbf{k}'-\mathbf{k}_v}}} \langle \psi_{m\mathbf{k}'} | \partial_{\mathbf{k}'-\mathbf{k}_v} V | \psi_{n\mathbf{k}} \rangle,$$

(S34)

Eq. S34 shows the scattering process between the two Kohn-Sham (KS) states $m\mathbf{k}'$ and $n\mathbf{k}$. Also, the e-ph matrix elements can be written as [S31]:

$$g_{mn,\nu}(\mathbf{k}, \mathbf{q}) = \frac{1}{\sqrt{2\omega_{q\nu}}} \langle \psi_{m\mathbf{k}+\mathbf{q}} | \partial_{q\nu} V | \psi_{n\mathbf{k}} \rangle, \quad (\text{S35})$$

In **Eq. S35**, the phonon wave vector \mathbf{q} is equal to $\mathbf{k}' - \mathbf{k}$, and, accordingly, $g_{mn,\nu}(\mathbf{k}, \mathbf{q})$ is replaced by $g_{mn,\nu}(\mathbf{k}, \mathbf{k} + \mathbf{q})$. In **Eq. S35**, $\partial_{q\nu} V$ is the derivative of the self consistent (sc) potential relative to a phonon of wavevector \mathbf{q} , frequency $\omega_{q\nu}$ and ν as branch index. The wave function $\psi_{n\mathbf{k}}$ is for band n and wavevector \mathbf{k} with eigenvalues of $\varepsilon_{n\mathbf{k}}$. The electron self-energy (Σ^e) and the phonon self-energy (Σ^{ph}) at temperature T for semiconductors and metals are explained by [S32, S33]:

$$\Sigma_{nk}^e(\omega, T) = \sum_{m\nu} \int \frac{d\mathbf{q}}{\Omega_{BZ}} |g_{mn,\nu}(\mathbf{k}, \mathbf{q})|^2 \times \left[\frac{n_{q\nu}(T) + f_{m\mathbf{k}+\mathbf{q}}(T)}{\omega - (\varepsilon_{m\mathbf{k}+\mathbf{q}} - \varepsilon_F) + \omega_{q\nu} + i\delta} + \frac{n_{q\nu}(T) + 1 - f_{m\mathbf{k}+\mathbf{q}}(T)}{\omega - (\varepsilon_{m\mathbf{k}+\mathbf{q}} - \varepsilon_F) - \omega_{q\nu} + i\delta} \right] \quad (\text{S36})$$

$$\Sigma_{q\nu}^{\text{ph}}(\omega, T) = 2 \sum_{mn} \int \frac{d\mathbf{k}}{\Omega_{BZ}} |g_{mn,\nu}(\mathbf{k}, \mathbf{q})|^2 \times \left[\frac{f_{n\mathbf{k}}(T) - f_{m\mathbf{k}+\mathbf{q}}(T)}{-\omega - (\varepsilon_{m\mathbf{k}+\mathbf{q}} - \varepsilon_{n\mathbf{k}}) - i\delta} \right], \quad (\text{S37})$$

where the ε_F is the Fermi energy, $n_{q\nu}(T) = \frac{1}{\exp(\frac{\omega_{q\nu}}{T}) - 1}$ is the Bose-Einstein distribution, $f_{n\mathbf{k}}(T)$ is the occupation at wavevector \mathbf{k} and band n and δ is a small positive real number for avoiding numerical instability [S31]. The Ω_{BZ} is the volume of Brillouin zone (BZ) and integral extend over the Ω_{BZ} . The imaginary part of the electron self-energy (Σ^e) and phonon self-energy (Σ^{ph}) are considered to calculate electron and phonon line widths as [S34]:

$$\Sigma_{nk}'^e(\omega, T) = \pi \sum_{m\nu} \int \frac{d\mathbf{q}}{\Omega_{BZ}} |g_{mn,\nu}(\mathbf{k}, \mathbf{q})|^2 \times [n_{q\nu}(T) + f_{m\mathbf{k}+\mathbf{q}}(T)] \delta(\omega - (\varepsilon_{m\mathbf{k}+\mathbf{q}} - \varepsilon_F) + \omega_{q\nu}) + (n_{q\nu}(T) + 1 - f_{m\mathbf{k}+\mathbf{q}}(T)) \delta(\omega - (\varepsilon_{m\mathbf{k}+\mathbf{q}} - \varepsilon_F) - \omega_{q\nu}), \quad (\text{S38})$$

$$\Sigma_{qv}'^{ph}(\omega, T) = 2\pi \sum_{mn} \int \frac{dk}{\Omega_{BZ}} |g_{mn,\nu}(\mathbf{k}, \mathbf{q})|^2 \times [(f_{nk}(T) - f_{mk+q}(T))\delta(-\omega - (\varepsilon_{mk+q} - \varepsilon_{nk}))] \quad (\text{S39})$$

The e-ph coupling strength of phonon mode ν and wave vector \mathbf{q} is [S31]:

$$\lambda_{qv} = \frac{1}{N(\varepsilon_F)\omega_{qv}} \sum_{mn} \int \frac{dk}{\Omega_{BZ}} |g_{mn,\nu}(\mathbf{k}, \mathbf{q})|^2 \delta(\varepsilon_{mk+q} - \varepsilon_F) \delta(\varepsilon_{nk} - \varepsilon_F) \quad (\text{S40})$$

where $N(\varepsilon_F)$ is the density of states/spin at Fermi level.

S11 Scattering processes

The excited electrons by SPs lose their collective mode, when they are scattered by other electrons [S35]. In metals, the dephasing process creates non-thermal electrons with high-level energy above Fermi level named hot carriers (HCs) [S35]. Unlike metals, in semiconductors, the scattered excited electrons by SPs cannot receive enough energy to get dephased; therefore, generation of HC excitons cannot occur in semiconductors. Here, we show that HCs can be generated in 2D semiconductors when they are subjected to the external fields like strain and heat (temperature).

To characterize the scattering in the semiconductors, electron-phonon (e-ph) and electron-electron (e-e) interactions should be combined within the first-principles calculations. The imaginary part of self-energy for e-e ($\text{Im } \Sigma^{\text{e-e}}$) and e-ph ($\text{Im } \Sigma^{\text{e-ph}}$) interactions acquire the scattering rate of electrons (**Fig. 13**). We compute the total relaxation time (τ_{nk}), which is the scattering rate inverse for band n and k -point in the Brillouin zone (BZ) region.

Taking into consideration the e-ph and e-e interactions, the total relaxation time (τ_{nk}) is calculated using **Eq. S4** [S30]:

$$\tau_{nk} = [2/\hbar \text{Im} \sum_{n,k}^{e-e} \sum_{n,k}^{e-ph}]^{-1} \quad (\text{S41})$$

Figs. S6(A) and **S7(A)** show the scattering rate and relaxation time $\tau_{n,k}$ for both unstrained and strain structures ($\pm 6\%$ strain) taking into account both electron-electron (e-e) and e-ph interactions. As can be seen in **Fig. S6(A)**, the scattering rate of both unstrained and strained H-SiB at ground state (0 K) highlights the differences between these two nanostructures. In comparison to the strained structure, the scattering rate is relatively linear, constant, and smaller than for the unstrained structure. Since there is a higher e-ph interaction in the monolayers under tensile deformation in comparison to both unstrained and strained under compressive strain, the scattering rate of the structures subjected to the tensile strains is more significant than both the subjected ones to compressive strain and unstrained ones. Strained monolayers have higher scattering rate and lower relaxation time in comparison to the unstrained monolayers. The scattering rate in the tensile strained H-SiB structures is more significant than the compressive strained structures due to a higher e-ph interaction in the tensile strained samples. Therefore, strained H-SiB generates a greater transport in the system, which results in a significant illumination.

Beside of strain effect, understanding the effect of heat (temperature) on the exciton-plariton coupling and HC generation in 2D semiconductors motivated us to compute the temperature effect on the scattering rate and relaxation time of unstrained and strained 2D H-SiB structures.

Figs. S6(B-D) show the effect of temperature on the scattering rate on unstrained and strained H-SiB monolayers, respectively. As can be seen in these figures, the scattering rate increases with increasing the temperature in both strained and unstrained conditions. The e-e and e-ph scattering rates for HCs in unstrained H-SiB are relatively constant within -2 to 2 eV region, and start relaxation time of 24fs and 27fs at ground state, respectively [S30], our findings show smaller

relaxation time semiconductors (7fs for H-SiB), which happen due to the fact that semiconductors have smaller carrier mobility in comparison to Metals.

Table S3. Slope of parabolic shape of relaxation time ($\tau_{n,k}$) for unstrained and strained H-SiB monolayers at different temperatures. Since the magnitude of scattering rate is important, we removed the negative sign from the slopes.

H-SiB	0 K	100 K	200 K	300 K
Strained (-6%)	0.015	0.4	0.56	0.65
Unstrained	0.0006	0.2	0.3	0.42
Strained (+6%)	0.03	0.5	0.65	0.7

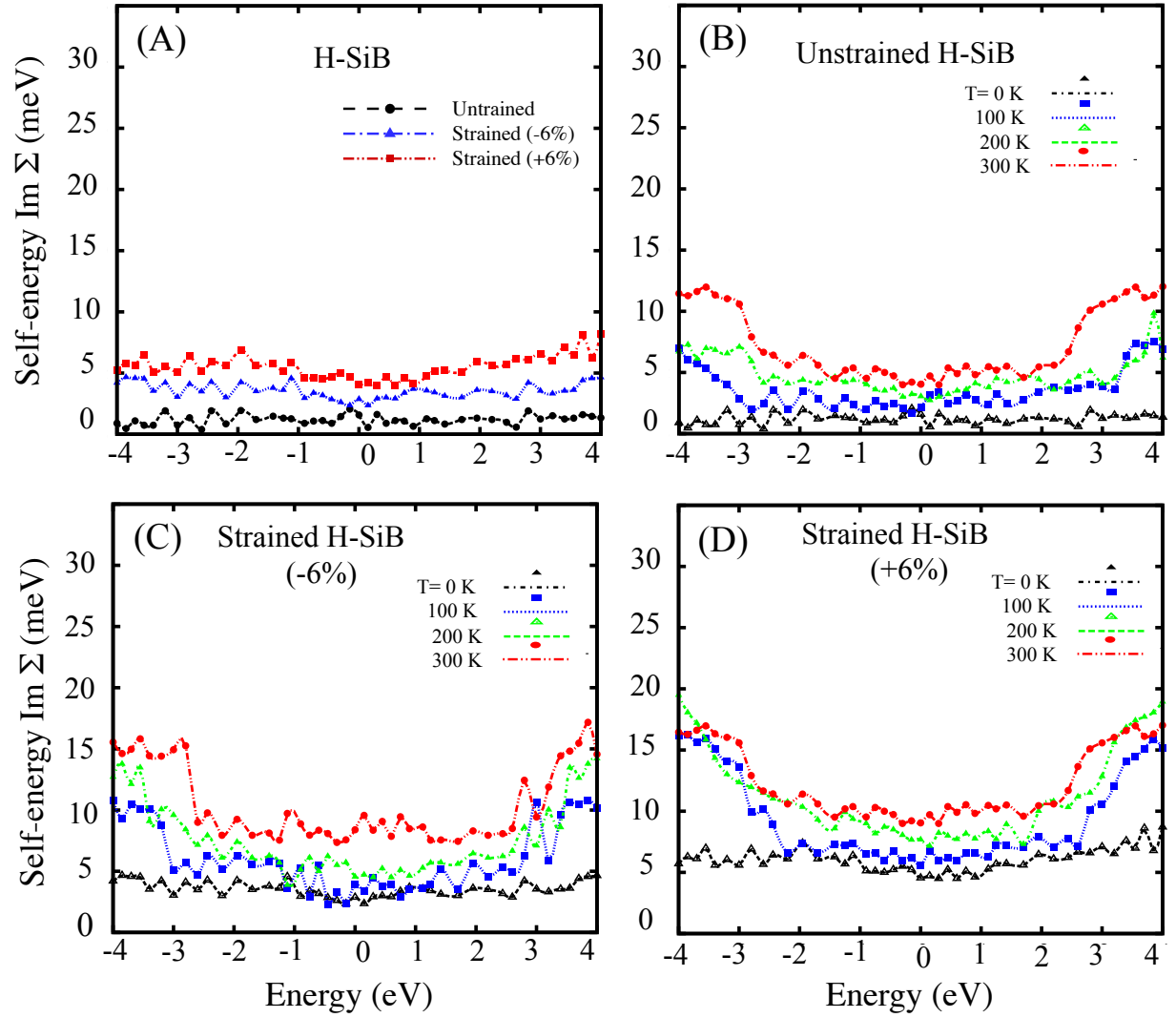


Fig. S6: Scattering rates or Imaginary part of self-energy ($\text{Im } \Sigma(\omega, q)$) within 4 eV of the Fermi energy for unstrained and strained H-SiB considering both e-e and e-ph interactions ($\text{Im } \Sigma^{\text{e-e}}(\omega, q) + \text{Im } \Sigma^{\text{e-ph}}(\omega, q)$).

growing outside of this region rapidly. Furthermore, in both strained and unstrained H-SiB monolayers, scattering rate increases with increasing the temperature; while the relaxation time decreases. The scattering rate of HCs in both unstrained and strained H-SiB indicates a parabolic behavior. As can be seen in **Fig. S6**, the slope of the scattering rate both unstrained and strained

structures increases with increasing temperature (**Table S3**). As reported in **Table S3**, the trend of slope of parabolic shape of $\tau_{n,k}$ for tensile strained H-SiB is more pronounced than two other structures at ground state and all the finite temperatures. Therefore, the highest scattering rate is for 6% strained structure at 300 K. It is due to the fact that with increasing temperature, the carrier mobility increases and scattering rate of carriers increase.

Let's assume that this scattering mechanism leads to the total relaxation time, as presented in **Figs. S6(B-D)**. The more scattered HCs exhibit the less relaxation time. The transport of electrons ($I(E)$) is commensurate with their scattering rate as $I(E) = \frac{e}{h} Tr(\Sigma A - \Gamma G^n)$, where Σ is the self-energy, Γ is the broadening matrix ($\Gamma = i(\Sigma - \Sigma^\dagger)$), A is the spectral function ($A = i(G - G^\dagger)$), and G is the Green's function of system as $G = (E - H - \Sigma)^{-1}$ [S36]. **Fig. S6** suggests that self-energy of H-SiB enhances by temperature, which results to large transmission.

As can be seen in **Figs. S7(B-D)**, a parabolic shape of relaxation time decays rapidly with increasing temperature for unstrained and strained (both tensile and compressive) monolayers. By increasing temperature, the slope of scattering rate (as can be seen in **Fig. S6**) increases. Additionally, due to the parabolic nature of scattering rate curves, by moving far from the Fermi energy (set to zero here) increases. Relaxation time function is proportional to the inverse of scattering rate. Therefore, by increasing the temperature, the relaxation time reduces. For instance, the average relaxation time at ground state is 7fs for unstrained, 5.75fs for compressive strained; and 5fs for tensile strained structures. In comparison to Au and Ag, which have a total which have a total relaxation time of 24fs and 27fs at ground state, respectively [S22], our findings show smaller relaxation time semiconductors (7fs for H-SiB), which happens due to the fact that semiconductors have smaller carrier mobility in comparison to Metals.

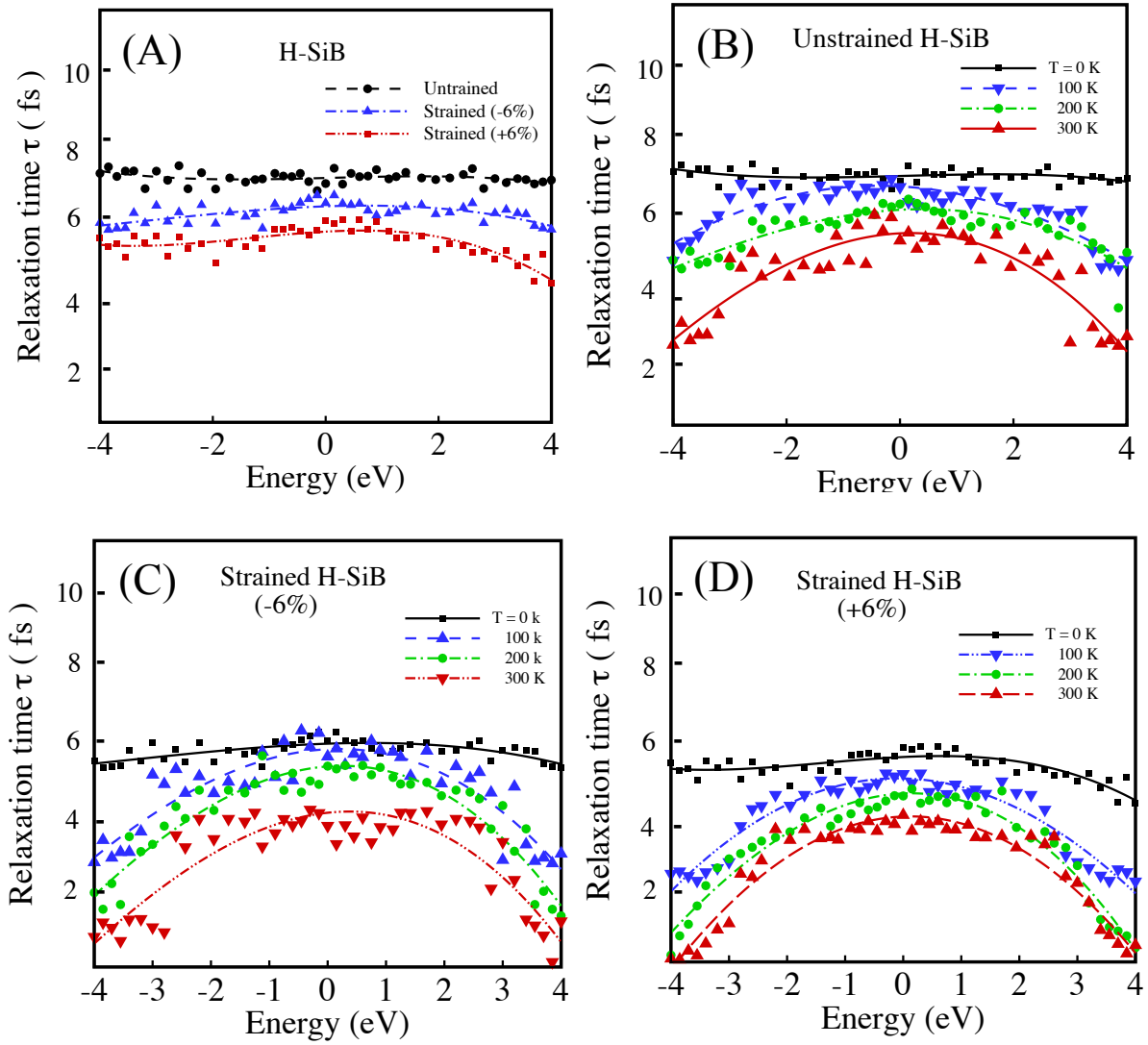


Fig. S7: Relaxation time (τ) within 4 eV for HCs in (A) unstrained at ground state, (B) unstrained at different temperatures, (C) strained H-SiB at 6% compressive strain at different temperatures, and (D) (C) strained H-SiB at 6% tensile strain at different temperatures.

S12 Light emission

The Green's function and BSE are utilized to compute the light absorption and emission, which

are, both, related to the polarization functions [S37]. We used non-equilibrium BSE to take into account the e-h interactions in the calculations [S38].

In the limit of low excitations (Tamm-Dancoff approximation) [S39, S40], the luminescence power spectrum becomes [S41]:

$$I(\omega) \propto \sum_{\lambda} |\chi_{\lambda}|^2 f_{\lambda}^< \delta(\omega - E_{\lambda}) \quad (\text{S42})$$

where E_{λ} is the eigenvalues of non-equilibrium BSE, χ_{λ} represents the exciton dipole matrix, and $f_{\lambda}^< \simeq n_B(E_{\lambda}, T)$ is the excitonic occupations with a Bose-Einstein distribution in the emission spectrum.

Scattering with phonons. To include the e-ph coupling in the calculations, we modified the Hamiltonian as [S42]:

$$\hat{H}_{el-ph} = \frac{1}{\sqrt{N_p}} \sum_{k,q} g_{mnv}(\mathbf{k}, \mathbf{q}) \hat{c}_{m\mathbf{k}+\mathbf{q}}^{\dagger} \hat{c}_{n\mathbf{k}} (\hat{a}_{\mathbf{q}v} + \hat{a}_{-\mathbf{q}v}^{\dagger}) \quad (\text{S43})$$

where $\hat{c}_{m\mathbf{k}}^{\dagger}$ is the fermionic (bosonic) creation, $\hat{c}_{n\mathbf{k}} (\hat{a}_{-\mathbf{q}v}^{\dagger} / \hat{a}_{\mathbf{q}v})$ is the annihilation operators with momentum \mathbf{k} (\mathbf{q}), N_p the number of unit cells. Here, the e-ph Hamiltonian (**Eq. S43**) is solved in a time-dependent perturbation theory with an excitonic particle basis [S40]. Then, with taking into consideration of the derivative of the dipole matrix, the phonon-assisted luminescence is identified as [S42]:

$$I^{BSE}(\omega; T) = \sum_{\mu\nu} \frac{\partial^2 |\chi_{\lambda}|^2}{\partial x_{\nu}^2} f_{\lambda}^< \left[\delta(\omega - E_{\lambda} - \omega_{\nu}) \frac{n_B(\omega_{\nu}; T)}{2\omega_{\nu}} + (\omega - E_{\lambda} + \omega_{\nu}) \frac{n_B(\omega_{\nu}; T)}{2\omega_{\nu}} \right] + \sum_{\lambda} |\chi_{\lambda}|^2 f_{\lambda}^< \delta(\omega - E_{\lambda}) \quad (\text{S44})$$

where x_v is the atomic displacement associated with the phonon mode with frequency ω_v , and n_B is the Bose distribution function. The first term in **Eq. S44** describe the absorption of a phonon, the second term is the emission of a phonon, and the third term is the light emission without phonons [S42, S44]. It should be notified that in **Eq. S44**, the third term vanishes in the case of materials with indirect gap [S42].

S13 Decay rate and hot carrier generation

To study SPP-electron coupling in the semiconductors, we developed a framework of perturbation theory and Feynman diagram for 2D semiconductors. To get decay rate $\Gamma(q_p, E_p)$ for a boson with an energy of E_p , and momentum q_p to electron-hole pairs, we calculated the imaginary part of the self-energy using **Eq. S45** [S30]:

$$\Gamma(q_p, E_p) = \frac{2\pi}{\hbar} \sum_{n,n',k} |g_{n,n',k}(q_p, E_p)|^2 \frac{1}{\pi} \text{Im} \left[\frac{f_{n,k} - f_{n,k+q_p}}{E_p(q_p) - (E_{n',k+q_p} - E_{n,k}) - i\eta} \right] \quad (\text{S45})$$

Where $g_{n,n',k}(q_p, E_p)$ is the coupling matrix for boson-electron interactions (for more details see the method section), $-E_{n,k}$ is the QP energies of hot hole in crystal momentum $-k$, and a state with band n . $E_{n',k+q_p}$ is a hot electron in crystal momentum $k+q_p$, and a state with band n_0 . Fermi occupations are stated by $f_{n,k}$ and $f_{n,k+q_p}$ with a small broadening η [S18]. In **Eq. S45**, the summation on n , n' , and k states is the transitions from empty to occupied states, which defers with $\hbar q_p$ in a crystal momentum, and E_p in energy [S30]. If the coupling matrix $g_{n,n',k}(q_p, E_p)$ in **Eq. S45** becomes weak, the imaginary part of polarizability $\text{Im} \chi(q_p, E_p)$ will dominate the decay rate of SPP.

The decay of excitation carriers gives generation rate $N_e(E)$ of hot holes and electrons with the energy E [S19]:

$$N_e(E) = \frac{2\pi}{\hbar} \sum_{n,n',k} |g_{n,n',k}(q_p, E_p)|^2 \frac{1}{\pi} \text{Im} \left[\frac{f_{n,k} - f_{n,k+q_p}}{E_p(q_p) - (E_{n',k+q_p} - E_{n,k}) - i\eta} \right] \delta(E - \epsilon_p) \quad (\text{S46})$$

where $|g_{n,n',k}(q_p, E_p)|^2$ is the Bose-electron coupling matrix as discussed in the methods

Section. Finally, the total HC generation is given by [S19]:

$$N_{\text{tot}} = \int_{E+\delta E}^{\infty} N_e(E) dE \quad (\text{S47})$$

where $N_e(E)$ is the rate of hot electrons.

Supporting References:

- S1. Gonze, X, Lee, C. Dynamical matrices, Born effective charges, dielectric permittivity tensors, and interatomic force constants from density-functional perturbation theory, *Phys. Rev. B* 1997; 55(16), 10355-10368.
- S2. Giannozzi P, Baroni S, Bonini N et al. QUANTUM ESPRESSO: a modular and open-source software project for quantum simulations of materials, *J. Phys.: Condens. Matter* 2009; 21(39), 395502.
- S3. Trullier N, Martins JL. Efficient pseudopotentials for plane-wave calculations, *Phys. Rev. B* 1991; 43(3), 1993-2006.
- S4. Hasegawa H, Kobayashi K, Takahashi Y, Harada J, Inabe T. Effective band gap tuning by foreign metal doping in hybrid tin iodide perovskites, *J. Mater. Chem. C* 2017; 5, 4048-4052.
- S5. Aierken Y, Leenaerts O, Peeters FM. A first-principles study of stable few-layer pentasilicene, *Phys. Chem. Chem. Phys* 2016; 18, 18486-18492.
- S6. Kuila T, Bose S, Mishra AK, Khanra P, Kim NH, Lee JH. Chemical functionalization of graphene and its applications, *Prog. Mater Sci* 2012; 57, 1061-1105.
- S7. Craciun MF, Khrapach I, Barnes MD, Russo S. Properties and applications of chemically functionalized graphene, *J. Phys.: Condens. Matter* 2013; 25, 423201.
- S8. Sharifzadeh S. Many-body perturbation theory for understanding optical excitations in organic molecules and solids. *J. Phys.: Condens. Matter* 2018; 30, 153002.
- S9. Hybertsen MS and Louie SG. Electron correlation in semiconductors and insulators: Band gaps and quasiparticle energies, *Phys. Rev. B* 1986; 34, 5390.
- S10. Shi G and Kioupakis E. Electronic and optical properties of nanoporous silicon for solar-cell applications, *ACS Photonics* 2015; 2 (2), 208–215.
- S11. Sharifzadeh S, Wong CY, Wu H, Cotts BL, Kronik L, Ginsberg NS and Neaton JB. Relating the Physical Structure and Optoelectronic Function of Crystalline TIPS-Pentacene, *Adv. Funct. Mater* 2015; 25, 2038-2046.
- S12. Rohlfing M and Louie SG. Electron-hole excitations and optical spectra from first principles, *Phys. Rev. B* 2000; 62, 4927 (2000).
- S13. Deslippe J, Samsonidze G, Strubbe DA, Jain M, Cohen ML and Louie SG. BerkeleyGW: A massively parallel computer package for the calculation of the quasiparticle and optical properties of materials and nanostructures, *Comput. Phys. Comm* 2012; 183, 1269–1289.
- S14. International A.S.T.M. ASTM G173-03-Standard Tables for Reference Solar Spectral Irradiances: Direct Normal and Hemispherical on 37 Tilted Surface 2012.

S15. Welch A.W, Baranowski L.L, Peng H, Hempel H, Eichberger R, Unold T, Lany S, Wolden C, Zakutayev A. Solar Cells: Trade-offs in thin film solar cells with layered chalcostibite photovoltaic absorbers, *Adv. Energy Mater.* 2017; 11.

S16. Das S, Pandey D, Thomas J, Roy T. The Role of Graphene and Other 2D Materials in Solar Photovoltaics, *Adv.Mater.* 2019; 31, 1802722.

S17. Zólyomi V, Wallbank JR and Fal'ko VI. Silicane and germanane: tight-binding and first-principles studies. *2D Materials* 2014; 1, 011005.

S18. Torbatian Z, Asgari R. Plasmonic physics of 2D crystalline materials, *Appl. Sci* 2018; 8, 238.

S19. Giuliani GF, Vignale G. Quantum Theory of the Electron Liquid; Cambridge University Press: *Cambridge, UK*, 2005.

S20. Adler SL. Quantum theory of the dielectric constant in real solids. *Phys. Rev* 1962; 126, 413.

S21. Pijpers J.J.H, Milder M.T.W, Delerue C, Bonn M, (Multi)exciton Dynamics and Exciton Polarizability in Colloidal InAs Quantum Dots. *J. Phys. Chem. C* 2010; 114, 6318.

S22. L. Hedin, S. Lundqvist, Effects of Electron-Electron and Electron-Phonon Interactions on the One-Electron States of Solids. in *Solid State Physics*, ed. by H. Ehrenreich, F. Seitz, D. Turnbull, Academic, New York, 1969, 23, 1-181.

S23. C. Delerue, M. Lannoo, G. Allan, Calculations of the electron-energy-loss spectra of silicon nanostructures and porous silicon. *Phys. Rev. B* 1997, 56, 15 306.

S24. Petersilka M, Gossmann UJ, Gross EKV. Excitation energies from time-dependent density-functional theory. *Phys. Rev. Lett* 1996; 76, 1212.

S25. Bernardi M, Vigil-Fowler D, Lischner J, Neaton JB, Louie, SG. Ab initio study of hot carriers in the first picosecond after sunlight absorption in Silicon. *Phys. Rev. Lett* 2014; 112, 257402.

S26. Noffsinger J, Giustino F, Malone BD, Park CH, Louie SG, Cohen ML. EPW: A program for calculating the electron–phonon coupling using maximally localized Wannier functions, *Comput. Phys. Comm* 2010; 181 (12), 2140–2148.

S27. Marzari N, Vanderbilt D. Maximally localized generalized Wannier functions for composite energy bands. *Phys. Rev. B* 1997; 56, 12847.

S28. Birch F. Equation of state and thermodynamic parameters of NaCl to 300 kbar in the high-temperature domain. *J. Geophys. Res. B* 1986; 83, 1257-1268.

S29. Poncé S, Margine ER, Verdi C, Giustino F. EPW: Electron–phonon coupling, transport and superconducting properties using maximally localized Wannier functions, *Comput. Phys. Comm* 2016; 209, 116-133.

- S30. Bernardi M, Mustafa J, Neaton JB and Louie SG. Theory and computation of hot carriers generated by surface plasmon polaritons in noble metals. *Nat. Comm* 2015; 6, 7044.
- S31. Poncé S, Margine ER, Verdi C and Giustino F. EPW: Electron–phonon coupling, transport and superconducting properties using maximally localized Wannier functions, *Comput. Phys. Comm* 2016; 209, 116-133.
- S32. Noffsinger J, Giustino F, Malone BD, Park CH, Louie SG and Cohen ML. EPW: A program for calculating the electron–phonon coupling using maximally localized Wannier functions, *Comput. Phys. Comm* 2010; 181 (12), 2140–2148.
- S33. Giustino F. Electron-phonon interactions from first principles. *Rev. Mod. Phys* 2017; 89, 015003.
- S34. Giustino F, Cohen ML and Louie SG. Electron-phonon interaction using Wannier functions, *Phys. Rev. B* 2007; 76, 165108.
- S35. Cushing SK. Plasmonic hot carriers skip out in femtoseconds. *Nat. Photonics* 2017; 11, 748–749.
- S36. Papior N, Lorente N, Frederiksen T, García A, Brandbyge M. Improvements on non-equilibrium and transport Green function techniques: The next-generation transiesta, *Comput. Phys. Comm* 2017; 212, 8-24.
- S37. Martin RM, Reining L and Ceperley DM. Ceperley. *Interacting Electrons*, Cambridge University Press, Cambridge 2016; *U.K.*
- S38. Strinati G. Application of the Green’s functions method to the study of the optical properties of semiconductors, *Riv. Nuovo Cimento* 1988; 11, 1.
- S39. Pfeiffer W, Kennerknecht C, Merschdorf M. Electron Dynamics in Supported Metal Nanoparticles: Relaxation and Charge Transfer Studied by Time-Resolved Photoemission. *Appl. Phys. A: Mater. Sci. Process* 2004; 78, 1011-1028.
- S40. Novoselov, KS, Geim, AK, Morozov S, Jiang D, Katsnelson MI, Grigorieva I, Dubonos S and Firsov AA. Two-dimensional gas of massless Dirac fermions in graphene. *Nature* 2005; 438, 197-200.
- S41. Schleife A, Rödl C, Fuchs F, Hannewald K and Bechstedt F. Optical absorption in degenerately doped semiconductors: Mott transition or Mahan excitons, *Phys. Rev. Lett.* 2011; 107, 236405.
- S42. Cannuccia E, Monserrat B. and Attacalite C. Theory of phonon-assisted luminescence in solids: Application to hexagonal boron nitride, *Phys. Rev. B* 2019; 99, 081109(R).

S43. Abt R, Ambrosch-Draxl C and Knoll P. Optical response of high temperature superconductors by full potential LAPW band structure calculations, *Physica B* 1994;1451–1452.

S44. Ehrenreich H and Cohen MH. Self-consistent field approach to the many-electron problem, *Phys. Rev.* 1959; 115, 786-790.